Electronic Supplementary Material (ESI) for Soft Matter.

Microdroplet self-propulsion during dropwise condensation on lubricant-infused surfaces

Jianxing Sun[a], Patricia Weisensee[a,b,*]

[a] Department of Mechanical Engineering & Materials Science, Washington University in St. Louis, MO
[b] Institute of Materials Science and Engineering, Washington University in St. Louis, USA

* corresponding author: p.weisensee@wustl.edu

Content

S1: Determination of initial lubricant layer thickness

S2: 3D confocal fluorescence measurement for lubricant thickness characterization

S3: Droplet immersion into lubricant layer

S4: Vapor condensation on vertical samples

S5: Adapted Neumann triangle

Movie 1: Droplet mobility in oil-rich and oil-poor regions

Movie 2: Droplet movement during vapor condensation on a vertical sample

Movie 3: Tack of microdroplet self-propulsion (with Fig. 5b)

Movie 4: Comparison of droplet dynamics on LIS with different oil viscosity

S1. Determination of initial lubricant layer thickness

We use high-speed interferometry to observe the early stages of vapor condensation to estimate the initial oil film thickness. First, we focus the 50x interferometry objective on the oil-air interface. The uniform black-white interference patterns seen in Fig. S1a originate from a slightly misaligned (*i.e.*, tilted) sample holder with respect to the objective. Next, we gently blow water vapor over the sample at very low flow rates (2 LPM). As shown in Fig. S1b, nucleated droplets appear, but do not interrupt the interference patterns, which means the droplets are still fully immersed in the lubricant layer. Anand *et al*. showed that submerged droplets are spherical.[1] As condensation proceeds, the droplets grow mainly through coalescence. When the droplets grow large enough and protrude the oil-air interface, small circular interference fringes form (red circles in Fig. S1c). We measure the droplet diameter D at this instance and assume that it is equal to the initial oil film thickness h_{oil}, based on the spherical geometry of the droplets. The main measurement error sources are from the uncertainties on profiles of condensed microdroplets and the misalignment between sample surface and the objective, which adds to an overall uncertainty of approximately ± 3 pixels (≈ ± 1.2 µm) for the Photron high-speed camera and ± 10 pixels (≈ ± 0.3 µm) for the Amscope camera with the 50x objective.

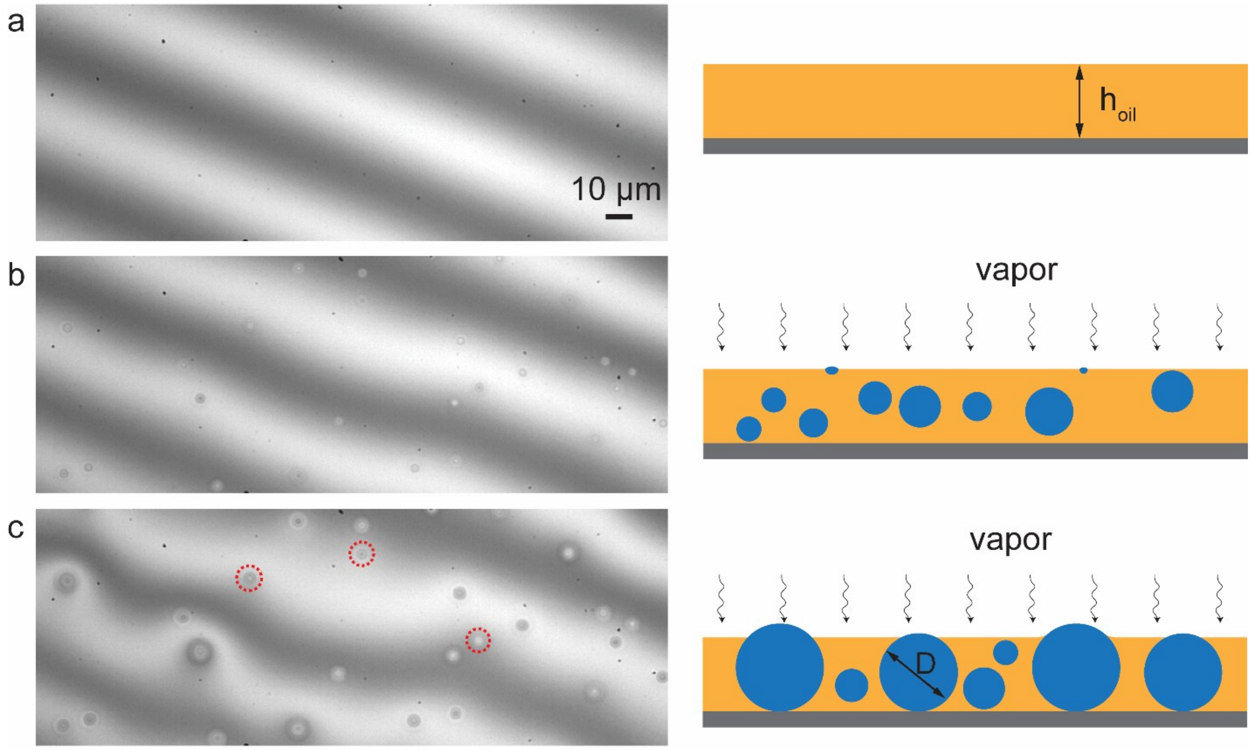

Fig. S1 Determination of initial oil film thickness using high-speed interferometry imaging. (a) Smooth oil-air interface before vapor condensation. (b) Small condensed droplets are fully immersed in the oil film. (c) The condensed droplets start to protrude the oil-air interface (red circles), at which point we measure the droplet size D and set it equal to the initial oil film thickness h_{oil}.

S2. 3D confocal fluorescence measurement for lubricant thickness characterization

To obtain the absolute thickness of the lubricant at later stages during condensation (*i.e.*, after lubricant re-distribution), we used scanning confocal fluorescence microscopy (Zeiss LSM 880 Airyscan Confocal Microscope) to measure the film thickness in oil-rich and oil-poor regions separately. Vacuum pump oil (Cole Parmer CP500) was used for this measurement and dyed with Lumogen F Red 305 (BASF Colors & Effects). We infused a Glaco-coated glass slide with the pump oil at 2500 rpm. Then, we conducted water vapor condensation experiment under the microscope. A 561 nm laser was used and the resolution in the vertical direction (Z stack) was set at 0.2 µm/slice. Fig. S2a shows a confocal microscope image of the oil film on LIS after two sweeping cycles. The red fluorescence signals represent the vacuum pump oil. We determined the oil film thickness of the oil-rich region surrounding a droplet with $D \approx 37$ µm (Fig. S2b) to $h_{\text{rich}} \approx 12 \pm 0.3$ µm. In the oil-poor regions (Fig. S2c), we found an oil film thickness of only $h_{\text{poor}} \approx 3 \pm 0.3$ µm.

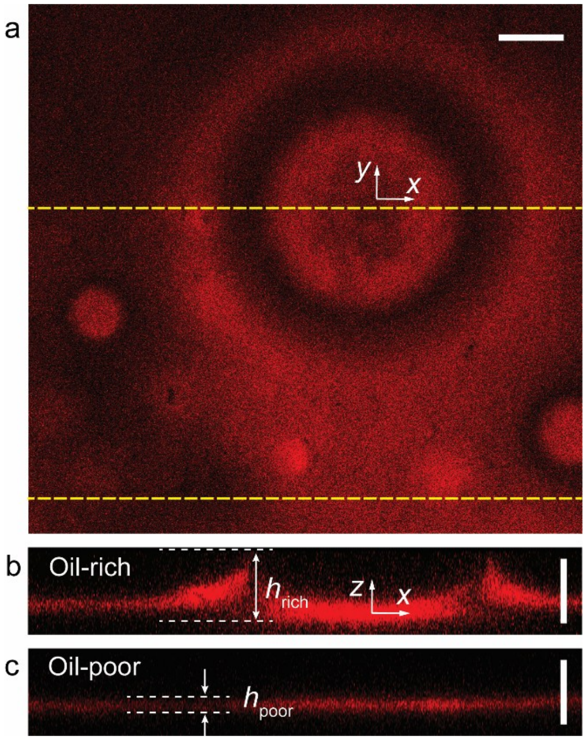

Fig. S2 Characterization of the oil film thickness in the oil-rich and oil-poor regions. (a) Top-view of a confocal microscope image after two condensation sweeping cycles. Fluorescence signals (red) show the vacuum pump oil, whereas droplets appear as empty spaces (black; no dye). (b) Cross-sectional view of a condensed droplet ($D \approx 37$ µm) and the oil film, corresponding to the upper yellow dashed line in (a). h_{rich} is defined as the oil film thickness at the apparent lubricant-droplet contact line. (c) Cross-sectional view of the oil film in the oil-poor region along the lower line in (a). Scale bars are 10 µm.

S3. Droplet immersion into lubricant layer

During self-propulsion of microdroplets, we observed that the majority of moving droplets fully immersed into the oil ridges of stationary droplets. To confirm our initial observation, we turned off the vapor supply after a period of vapor condensation to stop re-nucleation in the transition regions. Then, we focused on a large droplet surrounded by smaller droplets, which were either arrested at various distances from the larger droplet (black circles in Fig. S3a) or were still moving towards the larger droplet (yellow circles in Fig. S3a). We used high-speed interferometry to inspect the meniscus smoothness near these droplets. Fig. S3a shows the interference fringes nearby a stationary big droplet by lifting the focus plane of the microscope. From section S1 of the SI, we know that the inference fringes of the oil meniscus will be interrupted by the existence of partially immersed (*i.e.*, partially protruding) droplets, as shown in Fig. S3b. When the self-propulsion of a small moving droplet ends, the fringe pattern is ordered and parallel, which indicates that the droplet is fully immersed in the oil ridge. We also note that larger droplets do not fully immerse, since their size is larger than the meniscus height surrounding the big droplet.

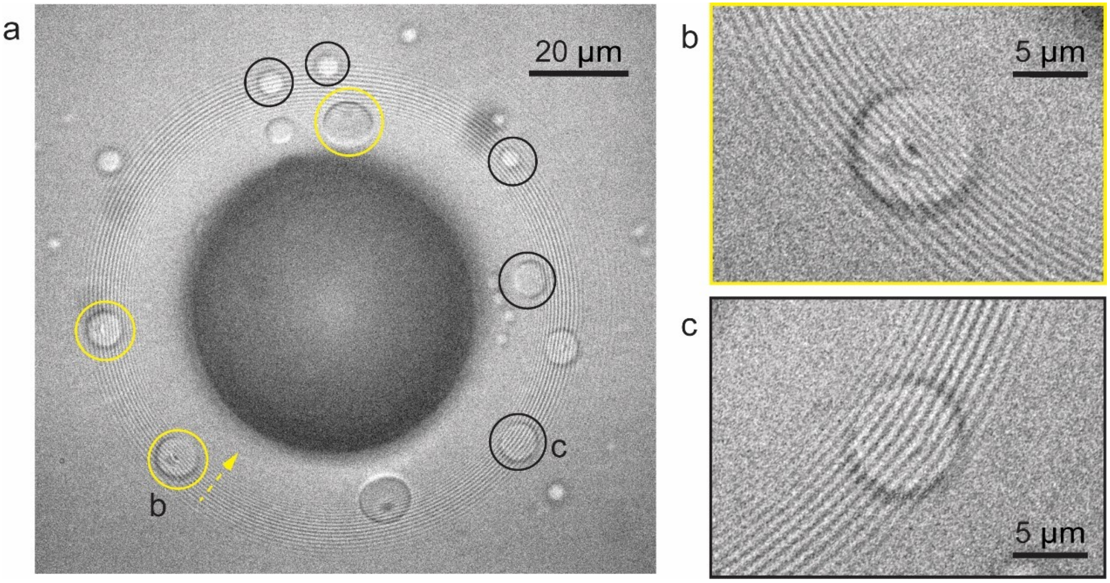

Fig. S3 Visualization of microdroplets immersed into the oil ridge surrounding a large pseudo-stationary droplet. (a) Interference patterns around a static droplet surrounded by several small droplets. (b) Interference patterns of the meniscus near a moving droplet (yellow circles in (a)). (c) Interference patterns of the meniscus near a static, fully submerged droplet (black circles in (a)).

S4. Vapor condensation on vertical samples

To verify that the microdroplet movement reported in the main manuscript is independent of gravity, we conducted additional vapor condensation experiments on a vertical sample. The setup is shown in Fig. S4. We observed the same movement of microdroplets as that on horizontal substrates (see **Movie S2**). However, once droplet sizes approach the capillary length, gravity comes into effect and droplets slide down, *i.e.*, naturally sweep the surface. We notice a decrease in the oil thickness in the trail of the sliding droplet, which enhances nucleation and the formation of more oil-rich regions.

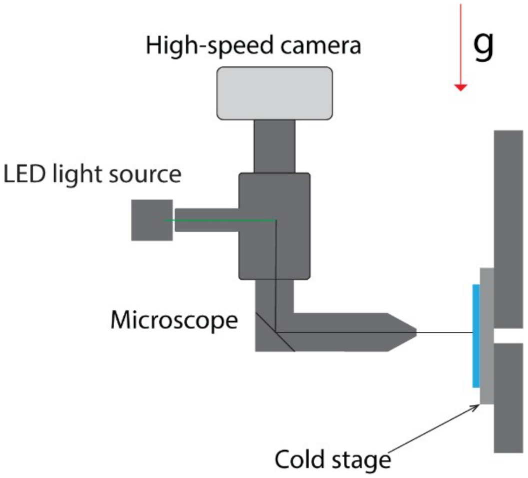

Fig. S4 Simplified schematic of the vertical setup

S5. Adapted Neumann triangle

For a non-cloaking oil, the water droplet (w), the oil meniscus (o), and the surrounding vapor/air (a) meet at the fluid three-phase contact line. The angles between these phases are given by the Neumann triangle[2]:

$$\cos\Theta_{w} = \frac{\gamma_{oa}^{2} - \gamma_{wa}^{2} - \gamma_{wo}^{2}}{2\gamma_{wo}\gamma_{wa}}, \quad \cos\Theta_{o} = \frac{\gamma_{wa}^{2} - \gamma_{oa}^{2} - \gamma_{wo}^{2}}{2\gamma_{wo}\gamma_{oa}}, \quad \cos\Theta_{a} = \frac{\gamma_{wo}^{2} - \gamma_{wa}^{2} - \gamma_{oa}^{2}}{2\gamma_{oa}\gamma_{wa}}. \tag{S1}$$

Here, Θ_w, Θ_o, Θ_a denote the angles inside the droplet, the oil meniscus, and the surrounding air phase, respectively (see inset of Fig. S5a). The Krytox GPL oils used in our experiments cloak water droplets due to a positive spreading coefficient, eliminating a direct three-phase liquid contact line.[3] The thickness of the cloaking layer was experimentally and theoretically reported on the scale of tens of nanometers.[1,4] Here, we will use an effective interfacial tension, $\gamma_{eff} = \gamma_{wo} + \gamma_{oa} - \delta$, at the droplet-lubricant-air interface, where δ is a function of the thickness of the nanoscopic oil wrapping layer.[5] We hypothesize that an adapted Neumann triangle is still applicable, where three surface tension vectors form a Neumann triangle, *i.e.*, $\vec{\gamma}_{eff} + \vec{\gamma}_{oa} + \vec{\gamma}_{wo} = 0$, and define the apparent 'three-phase' fluid contact line where the concave oil meniscus meets the convex droplet profile, as seen in Fig. S5a. The angle Θ_a can be experimentally measured from side-view images of microdroplets placed on LIS. Fig. S5b shows that Θ_a fluctuates between 140° and 160° for a wide range of droplet sizes. For the calculations presented in the main manuscript, we assume that Θ_a is constant and at 150°, independent of droplet size. With this insight, we can also compute the effective surface tension γ_{eff} and replace γ_w in equation eq. (S1) to calculate Θ_w

and Θ_o. Furthermore, we assume that the adapted Neuman triangle of a moving microdroplet will rotate with respect to the solid surface and the three angles remain constant.[6] Based on the geometry of the droplet, the apparent contact angle Θ_{app}, the meniscus angle of attack φ, and Θ_a have the relationship $\Theta_{app} = \varphi + (\pi - \Theta_a)$ at the apparent fluid contact line.

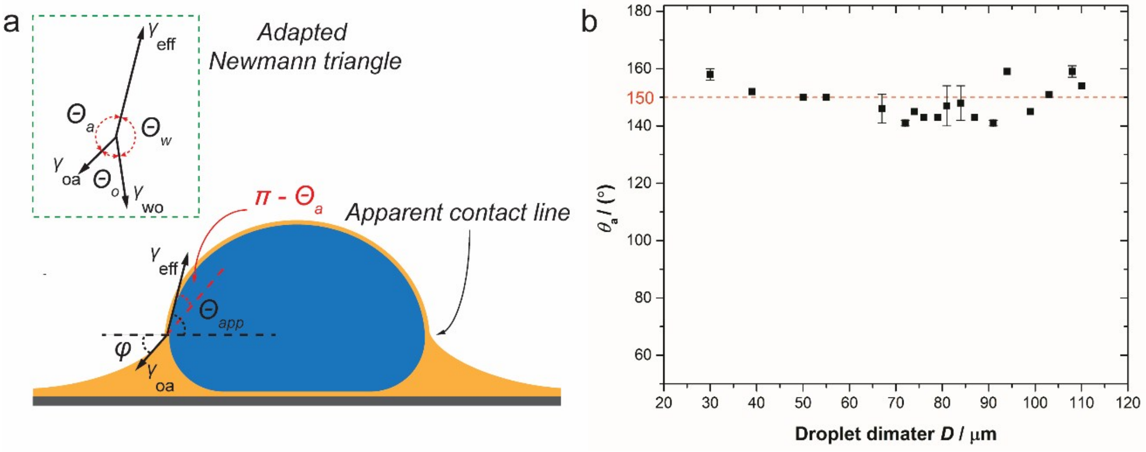

Fig. S5 Adapted Neumann triangle and measurements of the angle in the air phase Θ_a. (a) Schematic of an adapted Neumann triangle (insert) for a microdroplet with an oil cloaking layer. We assume an apparent contact line where the concave oil ridge meets the convex droplet profile. (b) Relationship of the adapted Neumann angle in the air phase Θ_a with droplet size. Black squares: experimental data for Θ_a. Red dash line: approximated average value from experimental data.

References

1 S. Anand, K. Rykaczewski, S. B. Subramanyam, D. Beysens and K. K. Varanasi, *Soft Matter*, 2015, **11**, 69–80.
2 M. Nosonovsky and R. Ramachandran, *Entropy*, 2015, **17**, 4684–4700.
3 D. Daniel, J. V. I. Timonen, R. Li, S. J. Velling and J. Aizenberg, *Nature Physics*, 2017, **13**, 1020–1025.
4 F. Schellenberger, J. Xie, N. Encinas, A. Hardy, M. Klapper, P. Papadopoulos, H.-J. Butt and D. Vollmer, *Soft Matter*, 2015, **11**, 7617–7626.
5 M. J. Kreder, D. Daniel, A. Tetreault, Z. Cao, B. Lemaire, J. V. I. Timonen and J. Aizenberg, *Physical Review X*, , DOI:10.1103/PhysRevX.8.031053.
6 M. Tress, S. Karpitschka, P. Papadopoulos, J. H. Snoeijer, D. Vollmer and H.-J. Butt, *Soft Matter*, 2017, **13**, 3760–3767.